

Integrated ultrafast all-optical polariton transistors

Pietro Tassan^{1,2,+}, Darius Urbonas^{1,+,#,*}, Bartos Chmielak³, Jens Bolten³, Thorsten Wahlbrink³, Max C. Lemme^{3,4}, Michael Forster⁵, Ullrich Scherf⁵, Rainer F. Mahrt¹, and Thilo Stöferle^{1,#,*}

¹ IBM Research Europe – Zurich, Rüschlikon, Switzerland

² Photonics Laboratory, ETH Zürich, Zürich, Switzerland, Switzerland

³ AMO GmbH, Aachen, Germany

⁴ Chair of Electronic Devices, RWTH Aachen University, Aachen, Germany

⁵ Macromolecular Chemistry Group and Wuppertal Center for Smart Materials & Systems (CM@S), Bergische Universität Wuppertal, Wuppertal, Germany

⁺ These authors contributed equally to this work.

[#] These authors have jointly supervised this work.

^{*} Corresponding authors: dar@zurich.ibm.com, tof@zurich.ibm.com

The clock speed of electronic circuits has been stagnant at a few gigahertz for almost two decades because of the breakdown of Dennard scaling¹, which states that by shrinking the size of transistors they can operate faster while maintaining the same power consumption. Optical computing could overcome this roadblock², but the lack of materials with suitably strong nonlinear interactions needed to realize all-optical switches has, so far, precluded the fabrication of scalable architectures. Recently, microcavities in the strong light-matter interaction regime enabled all-optical transistors³ which, when used with an embedded organic material, can operate even at room temperature with sub-picosecond switching times⁴, down to the single-photon level⁵. However, the vertical cavity geometry prevents complex circuits with on-chip coupled transistors. Here, by leveraging silicon photonics technology, we show exciton-polariton condensation at ambient conditions in micrometer-sized, fully integrated high-index contrast grating microcavities filled with an optically active polymer. By coupling two resonators and exploiting seeded polariton condensation, we demonstrate ultrafast all-optical transistor action and cascability. Our experimental findings open the way for scalable, compact all-optical integrated logic circuits that could process optical signals two orders of magnitude faster than their electrical counterparts.

All-optical logic with the ambition to supplement or even partly replace electrical circuits has been an active field of research for several decades^{2,6-8}. On this journey, a large variety of device concepts has been explored, including optical bistability in semiconductor quantum wells and other materials⁷, semiconductor optical amplifiers⁹, resonators based on rings¹⁰, discs¹¹ and photonic crystals¹², plasmonics¹³, Mach-Zehnder

interferometers¹⁴, excitons¹⁵ and single molecules¹⁶. However, only a few of them provided cascability and fan-out, while simultaneously allowing operation at speeds that significantly surpass current electronic circuits. Nevertheless, scalability towards many coupled all-optical gates has remained a persistent challenge, not only for free-space architectures¹⁷, but also because of the generally low material-intrinsic nonlinearities and/or the required size and precise matching of optical resonators across a chip¹⁸. Some recent approaches utilize the strong light-matter interaction regime, where an optically active material is embedded in a microcavity such that the coupling rate between optoelectronic excitations (correlated electron-hole pairs, excitons) in the material and photons in the cavity exceeds the loss rates in the material and the cavity¹⁹, effectively forming hybrid light-matter exciton-polariton quasi-particles. By using parametric scattering or resonant excitation, optical amplifiers²⁰ as well as transistors³ and routers^{21,22} have been realized at cryogenic temperature, and more recently with lead halide perovskites at room temperature²³. The large exciton binding energy in organics permits creating exciton-polaritons at room temperature²⁴. Moreover, the polariton formation can be enhanced by matching the detuning of the polariton state from the exciton reservoir to the energy of molecular vibrational modes²⁵. At sufficiently high excitation density, nonlinear polariton condensation occurs^{26,27} resulting in coherent, macroscopic occupation of a single polariton mode.

Light inserted into the cavity can seed and promote polariton condensation through bosonic stimulation, which can be harnessed for all-optical transistors and AND/OR logic gates⁴ operating at sub-picosecond speed and controlled with only a few signal photons⁵. A downside common to these exciton-polariton devices, however, is that they were based on vertical cavities with distributed Bragg reflectors (DBR) where the wavevector of the polariton condensate is essentially perpendicular to the substrate. Therefore, any emitted light to be used as input for other devices must be routed externally by free-space optics, inducing hundreds of picoseconds propagation delay between transistors and preventing a scalable architecture. Subwavelength gratings built from materials with high refractive index contrast provide an alternative to DBRs^{28,29} and have already been used in a vertical microcavity structure to realize exciton-polariton lasing³⁰. Fabricating a pair of high-contrast gratings (HCG) perpendicular to the chip substrate, Fabry-Pérot-like cavities can be created^{31,32} where the cavity mode is parallel to the substrate, enabling scalable in-plane architectures. Remarkably, compared to polariton condensation with metal^{33,34} and silicon³⁵ metasurfaces, where the condensate extends over hundreds of micrometers, the modal area in HCG cavities is only about $1 \mu\text{m}^2$, permitting extraordinarily compact optical circuits with high device densities beneficial for low power consumption and high speed.

Here, we establish polariton condensation at room temperature by introducing integrated HCG cavities filled with an organic ladder-type polymer. With one HCG cavity generating the control signal that constitutes the input and “seed” for a second “transistor” cavity, we demonstrate transistor action on a picosecond time scale. We observe up to 60x gain and a switching contrast exceeding 8:1, and this configuration implicitly showcases the cascability of the device.

On-chip polariton condensation

As illustrated in Fig. 1a, the device comprises two HCG mirrors, providing the lateral light confinement, and the polymer as active material simultaneously serving as a guiding layer for vertical light confinement by total internal reflection. The diameter and pitch of the grating silicon posts are chosen to yield high in-plane reflectivity for transverse-electric (TE) light polarization at incidence perpendicular to the grating (see Extended Data Fig. 1). The wide reflectivity maximum in spectrum and configuration space ensures broadband reflectivity and excellent robustness against fabrication errors. The HCG microcavity (Fig. 1b)

is fabricated on a silicon-on-insulator (SOI) wafer using state-of-the-art silicon photonics process technology (see Methods and Extended Data Fig. 2). The device is completed by spin-coating the ladder-type polymer layer, followed by an encapsulation step with a thin alumina layer. Photonic simulations (Fig. 1c-e) show the confinement of the optical mode within the device, resulting in a cavity quality factor of around $Q \sim 400$ at a wavelength near 490 nm, despite the strong optical absorption of silicon, which constitutes the HCGs. Notably, such Q -factor is sufficiently high to enable strong light–matter interaction but at the same time low enough to ensure sub-picosecond polariton lifetimes and to relax the fabrication tolerance requirements for matching resonator wavelengths across the chip.

We excite the structure with a focused beam from the top using a pulsed laser (see Methods). Above a threshold near $P_{\text{th}} = 50 \mu\text{J cm}^{-2}$, the emitted light intensity increases nonlinearly (Fig. 2a, top panel) and a sharp emission peak emerges from the broad photoluminescence background (Fig. 2a, inset). With increasing pump fluence the peak suddenly narrows from ~ 7 meV full-width at half-maximum (FWHM), which is consistent with the calculated Q -factor, down to ~ 2 meV while it continuously blue-shifts by about 5 meV from its original photon energy at a pump fluence of $120 \mu\text{J cm}^{-2}$ (Fig. 2a, bottom panel). To confirm that these observations are indeed signatures of polariton condensation, as already observed in vertical DBR cavities with the same active material²⁶, we measure a manifold of devices where the cavity length L is systematically varied. Plotting the resonance energies versus the cavity lengths, we observe the characteristic bending of the lower polariton branch in the strong light–matter interaction regime, which is supported by comparing to simulations of the weakly coupled and the polymer-filled cavities (Fig. 2b,c). Fitting with a coupled oscillators model (Extended Data Fig. 3) yields a Rabi splitting of $2\Omega = 327 \pm 48$ meV for an excitonic fraction of 50% at $L = 1.7 \mu\text{m}$. The large Rabi splitting and high excitonic fraction, compared to the values found in vertical DBR cavities where polariton condensation was observed²⁶ ($2\Omega \sim 120$ meV and 20% exciton fraction), can be understood from the significantly increased amount of polymer material in the cavity that is, however, partly offset by the reduced mirror finesse. Notably, polariton condensation occurs only when the lower polariton branch is within ± 20 meV the energy of the exciton reservoir (2.714 eV) minus the energy of the strong vibronic transition of the polymer⁵ (200 meV) where vibron-enhanced relaxation is prevalent³⁶.

Introducing a curvature to the HCGs allows us to engineer the modal structure of the microcavity. Gratings with a Gaussian shape, besides increasing the light confinement along the grating, lead to the discretization of the transversal modes (Extended Data Fig. 4). The different transversal orders can be clearly identified from the real-space emission patterns of the polariton condensates, which do not show the actual intracavity light field but the (parasitic) vertically scattered light from the HCGs. Thereby, by engineering the cavity length and curvature, we can ensure single mode polariton condensates with well-defined polarization (Extended Data Fig. 5), an important feature for controlled coupling of multiple HCG resonators. Furthermore, the resonance energies line up almost perfectly in this study of more than three hundred HCG cavities, providing confidence about the homogeneity, robustness, and scalability of the fabrication processes.

To realize ultrafast devices, it is important to assess the dynamics of the polariton condensation. Therefore, we performed experiments exciting a single HCG cavity with two subsequent excitation pulses of the same fluence and same duration (~ 150 fs) while controlling the variable time delay between them. When the fluence of a single pulse is below threshold, the polariton condensation process with its concomitant increase in emission is triggered only when the second pulse arrives within about 1 ps (Extended Data Fig. 6). For individual pulse fluences above threshold, a strong nonlinear intensity increase is observed when the second pulse comes within the first 1–2 ps, which we therefore attribute to the lifetime of the condensate. For larger time delays, a much longer lifetime component around 20 ps is observed that corresponds to the

lifetime of the exciton reservoir. Hence, from the time scale of the initial fast drop, the maximum repetition rate of the devices can be inferred, and the height of the long tail versus the initial peak gives a limit for the extinction.

Coupled cavities and transistor action

Next, we studied two coupled cavities with curved HCG mirrors, having the same resonance energy, separated by a 3 μm gap. We excited each with an ultrafast pulse of controlled fluence and a variable time delay between the two pulses (Fig. 3a). We used the output of one cavity, representing the control gate or “seed”, as input for the other cavity, representing the “transistor”. The polymer layer that covers both structures, as well as the space between them, serves as a waveguide. Notably the in-plane divergence of the light outcoupling from the seed cavity through the HCG mirror is low enough to couple sufficiently well into the same mode of the other cavity.

When exciting the transistor cavity below threshold ($P_{\text{transistor}} = 0.8 P_{\text{th}}$), real space images of the emission (Fig. 3b) show that the transistor can nevertheless attain polariton condensation, but only if the seed is excited above its condensation threshold ($P_{\text{seed}} = 1.2 P_{\text{th}}$) and has the ‘right’ timing with respect to the transistor excitation (more details follow below). We record the output intensity of the transistor cavity by collecting the emission spectrum only from the transistor HCG mirror that is on the far side from the seed, i.e. the transistor output. When we plot the emission versus the excitation fluence (Fig. 3c), we find that the condensation threshold is reduced only when the gating signal from the seed is present and arrives at the ‘right’ time.

To map the temporal dynamics, we vary both the transistor excitation fluence and the time delay between the excitation pulses for the seed and the transistor cavity, for a fixed seed excitation fluence of $P_{\text{seed}} = 1.5 P_{\text{th}}$ (Fig. 3d). Comparing the emission intensities, we observe that signal amplification (Fig. 3e) in the transistor only occurs when the seed cavity is excited ~ 1 ps before the transistor cavity (which corresponds to the ‘right’ timing mentioned above). We attribute this optimal timing condition to the time required for a single HCG cavity to condense. Furthermore, we observe a significant threshold reduction of the transistor cavity (Fig. 3e), which for this seed fluence is about 15%, but can reach more than 30% with stronger seed ($P_{\text{seed}} = 2 P_{\text{th}}$).

As both seed and transistor cavities are nominally identical, they can switch roles. When we detect the light on the HCG mirror of the seed on the far side of the transistor cavity, we observe the mirrored temporal dynamics compared to Fig. 3d (Extended Data Fig. 7). Effectively, this demonstrates that the excitation pulse sequence is defining the directional flow of the signal on the chip. Ultimately, this suggests that scalable circuits with multiple subsequent transistors requiring well-defined signal propagation without back-action can be achieved by a well-defined excitation sequence.

Discussion and conclusions

We extract key transistor metrics from the emission spectra and their temporal dynamics. When comparing the emission spectrum at the transistor output without and with applying the excitation to the transistor cavity (Fig. 4a, top panel), we see that the amplified peak faithfully reproduces the input from the seed, only mildly distorting its energetic position and spectral shape. Likewise, comparing spectra from the transistor output without and with seed excitation shows that the output spectrum remains essentially unchanged apart from the intensity change, allowing the extraction of the extinction ratio (on/off) of the

transistor (Fig. 4a, bottom panel). The unmodified spectrum is a fundamental requirement for the cascability of the devices. We plot the transistor metrics as a function of transistor excitation fluence (Fig. 4b), showing that for a given seed excitation fluence ($P_{\text{seed}} = 1.5 P_{\text{th}}$) the amplification increases with the transistor excitation up to a value of 43. The extinction peaks near the threshold at a ratio of 8:1. Varying the seed excitation fluence, and thereby the intensity of the gating input to the transistor, we find that the signal amplification increases for smaller input signals (Fig. 4c), reaching 60 for the smallest inputs that we could produce without losing polariton condensation in the seed cavity.

Furthermore, to assess the temporal robustness of the transistor amplification, we investigate how the amplification dynamics change with transistor excitation fluence (Fig. 4d). We find that the delay time between the seed and the transistor excitation where the maximum amplification is achieved slightly shifts from -0.9 ps to -1.4 ps with increasing transistor excitation. This can be understood considering that for stronger transistor excitation, the spontaneous polariton condensation is generally more dominant, and therefore the seed light has to be injected early enough into the cavity to stimulate scattering into the seeded mode and prevent spontaneous condensation.

In conclusion, we realized optically-pumped room-temperature polariton condensates that, in contrast to previous architectures, feature a single micrometer-sized condensate mode that is parallel to the substrate, enabling integrated planar circuits. By coupling two resonators, we demonstrated all-optical ultrafast transistor action and cascability of the device. Signal amplification of up to a factor of 60 enables large fan-out. Building on silicon photonics processing technology and exploiting the engineerability of the HCG cavities, we expect that our approach can be scaled to combine several transistors to logic gates⁴ and more complex logic circuits. Using waveguides with either HCGs³⁷ or silicon nitride co-integration^{38,39} would allow routing the signals between the transistors as well as the excitation pulses for the polariton condensates.

References

1. Dennard, R. H. *et al.* Design of ion-implanted MOSFET's with very small physical dimensions. *IEEE J. Solid-State Circuits* **9**, 256–268 (1974).
2. Miller, D. A. B. Are optical transistors the logical next step? *Nat. Photonics* **4**, 3–5 (2010).
3. Ballarini, D. *et al.* All-optical polariton transistor. *Nat. Commun.* **4**, 1778 (2013).
4. Zasedatelev, A. V. *et al.* A room-temperature organic polariton transistor. *Nat. Photonics* **13**, 378–383 (2019).
5. Zasedatelev, A. V. *et al.* Single-photon nonlinearity at room temperature. *Nature* **597**, 493–497 (2021).
6. Caulfield, H. J. Perspectives in optical computing. *Computer* **31**, 22–25 (1998).
7. Gibbs, H. *Optical Bistability: Controlling Light With Light*. (Elsevier, 1985).
8. Haus, H. A. & Whitaker, N. A. All-Optical Logic in Optical Waveguides. *Philos. Trans. R. Soc. Lond. Ser. Math. Phys. Sci.* **313**, 311–319 (1984).

9. Stubkjaer, K. E. Semiconductor optical amplifier-based all-optical gates for high-speed optical processing. *IEEE J. Sel. Top. Quantum Electron.* **6**, 1428–1435 (2000).
10. Almeida, V. R., Barrios, C. A., Panepucci, R. R. & Lipson, M. All-optical control of light on a silicon chip. *Nature* **431**, 1081–1084 (2004).
11. Liu, L. *et al.* An ultra-small, low-power, all-optical flip-flop memory on a silicon chip. *Nat. Photonics* **4**, 182–187 (2010).
12. Nozaki, K. *et al.* Sub-femtojoule all-optical switching using a photonic-crystal nanocavity. *Nat. Photonics* **4**, 477–483 (2010).
13. Fu, Y. *et al.* All-Optical Logic Gates Based on Nanoscale Plasmonic Slot Waveguides. *Nano Lett.* **12**, 5784–5790 (2012).
14. Tang, X. *et al.* A Reconfigurable Optical Logic Gate With up to 25 Logic Functions Based on Polarization Modulation With Direct Detection. *IEEE Photonics J.* **9**, 1–11 (2017).
15. Kuznetsova, Y. Y. *et al.* All-optical excitonic transistor. *Opt. Lett.* **35**, 1587–1589 (2010).
16. Hwang, J. *et al.* A single-molecule optical transistor. *Nature* **460**, 76–80 (2009).
17. McCormick, F. B. *et al.* Six-stage digital free-space optical switching network using symmetric self-electro-optic-effect devices. *Appl. Opt.* **32**, 5153–5171 (1993).
18. Fushimi, A. & Tanabe, T. All-optical logic gate operating with single wavelength. *Opt. Express* **22**, 4466–4479 (2014).
19. Kavokin, A. V. *et al.* *Microcavities*. (Oxford University Press, Oxford, New York, 2017).
20. Savvidis, P. G. *et al.* Angle-Resonant Stimulated Polariton Amplifier. *Phys. Rev. Lett.* **84**, 1547–1550 (2000).
21. Marsault, F. *et al.* Realization of an all optical exciton-polariton router. *Appl. Phys. Lett.* **107**, 201115 (2015).
22. Schmutzler, J. *et al.* All-optical flow control of a polariton condensate using nonresonant excitation. *Phys. Rev. B* **91**, 195308 (2015).

23. Feng, J. *et al.* All-optical switching based on interacting exciton polaritons in self-assembled perovskite microwires. *Sci. Adv.* **7**, eabj6627 (2021).
24. Lidzey, D. G. *et al.* Strong exciton–photon coupling in an organic semiconductor microcavity. *Nature* **395**, 53–55 (1998).
25. Coles, D. M. *et al.* Vibrationally Assisted Polariton-Relaxation Processes in Strongly Coupled Organic-Semiconductor Microcavities. *Adv. Funct. Mater.* **21**, 3691–3696 (2011).
26. Plumhof, J. D., Stöferle, T., Mai, L., Scherf, U. & Mahrt, R. F. Room-temperature Bose–Einstein condensation of cavity exciton–polaritons in a polymer. *Nat. Mater.* **13**, 247–252 (2014).
27. Daskalakis, K. S., Maier, S. A., Murray, R. & Kéna-Cohen, S. Nonlinear interactions in an organic polariton condensate. *Nat. Mater.* **13**, 271–278 (2014).
28. Mateus, C. F. R., Huang, M. C. Y., Yunfei Deng, Neureuther, A. R. & Chang-Hasnain, C. J. Ultrabroadband mirror using low-index cladded subwavelength grating. *IEEE Photonics Technol. Lett.* **16**, 518–520 (2004).
29. Chang-Hasnain, C. J. & Yang, W. High-contrast gratings for integrated optoelectronics. *Adv. Opt. Photonics* **4**, 379–440 (2012).
30. Zhang, B. *et al.* Zero-dimensional polariton laser in a subwavelength grating-based vertical microcavity. *Light Sci. Appl.* **3**, e135–e135 (2014).
31. Stöferle, T. *et al.* Ultracompact Silicon/Polymer Laser with an Absorption-Insensitive Nanophotonic Resonator. *Nano Lett.* **10**, 3675–3678 (2010).
32. Urbonas, D. Tunable coupled microcavities for enhanced light-matter interaction. (ETH Zurich, 2019). doi:10.3929/ethz-b-000382925.
33. Ramezani, M. *et al.* Plasmon-exciton-polariton lasing. *Optica* **4**, 31–37 (2017).
34. Hakala, T. K. *et al.* Bose–Einstein condensation in a plasmonic lattice. *Nat. Phys.* **14**, 739–744 (2018).
35. Castellanos, G. W., Ramezani, M., Murai, S. & Gómez Rivas, J. Non-Equilibrium Bose–Einstein Condensation of Exciton-Polaritons in Silicon Metasurfaces. *Adv. Opt. Mater.* **11**, 2202305 (2023).

36. Mazza, L., Kéna-Cohen, S., Michetti, P. & La Rocca, G. C. Microscopic theory of polariton lasing via vibronically assisted scattering. *Phys. Rev. B* **88**, 075321 (2013).
37. Urbonas, D., Mahrt, R. F. & Stöferle, T. Low-loss optical waveguides made with a high-loss material. *Light Sci. Appl.* **10**, 15 (2021).
38. Cegielski, P. J. *et al.* Monolithically Integrated Perovskite Semiconductor Lasers on Silicon Photonic Chips by Scalable Top-Down Fabrication. *Nano Lett.* **18**, 6915–6923 (2018).
39. Chauhan, N. *et al.* Ultra-low loss visible light waveguides for integrated atomic, molecular, and quantum photonics. *Opt. Express* **30**, 6960–6969 (2022).
40. Scherf, U., Bohnen, A. & Müllen, K. Polyarylenes and poly(arylenevinylene)s, 9 The oxidized states of a (1,4-phenylene) ladder polymer. *Makromol. Chem.* **193**, 1127–1133 (1992).
41. Liu, V. & Fan, S. S4 : A free electromagnetic solver for layered periodic structures. *Comput. Phys. Commun.* **183**, 2233–2244 (2012).

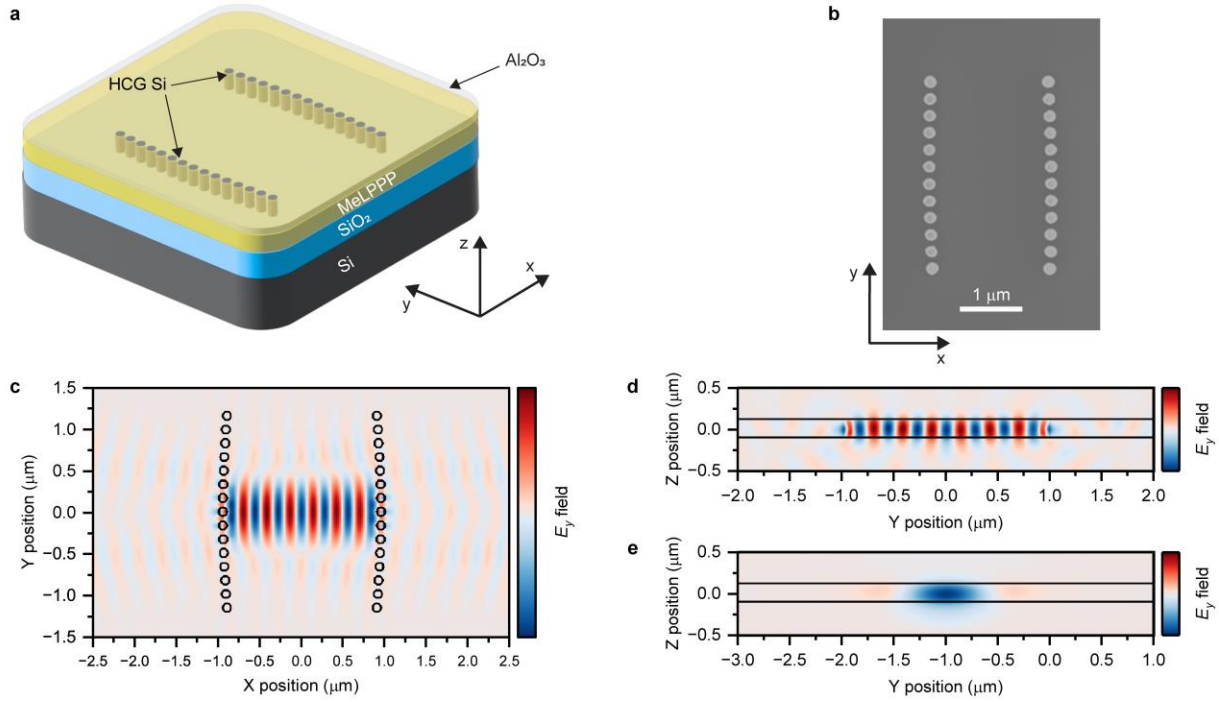


Fig. 1 | Integrated high contrast grating cavity. **a**, Sketch of integrated high contrast grating (HCG) cavity with the active polymer (MeLPPP) and encapsulation layer (Al₂O₃). **b**, Scanning electron microscopy image (top view) of a fabricated device. **c-e**, Different views of a three-dimensional finite-difference time-domain (3D FDTD) simulation of the field distribution of the resonant mode in the cavity. Overlaid in black are the outlines of the structure.

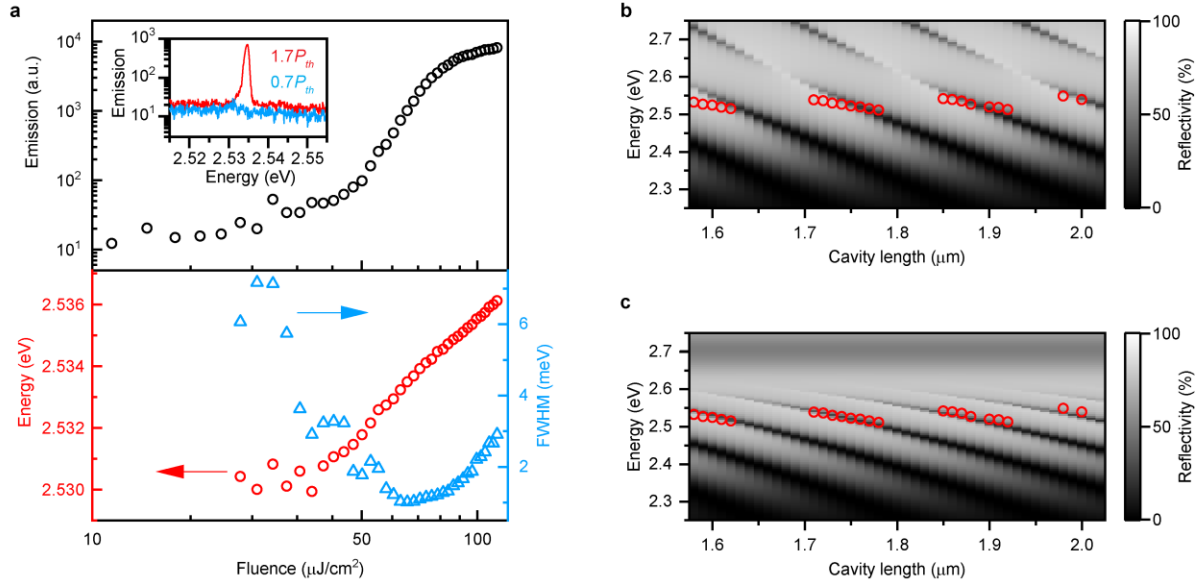


Fig. 2 | Strong light–matter interaction regime and polariton condensation. **a**, The top panel shows the emission as a function of excitation fluence. This light-in light-out characteristic exhibits a nonlinear increase above the threshold ($P_{\text{th}} \sim 50 \mu\text{J cm}^{-2}$) and saturation at higher fluences. The inset shows the emission spectra at $0.7 P_{\text{th}}$ (blue), and $1.7 P_{\text{th}}$ (red). The bottom panel displays the peak width and center energy of the emission peak as a function of excitation fluence, showing a sudden narrowing at the threshold and a continuous blue-shift above. **b**, Reflectivity (grey scale) obtained from a two-dimensional (2D) rigorous coupled wave analysis (RCWA) calculation as a function of cavity length in the weak coupling regime with refractive index $n = 1.86 = \text{const.}$ and $k = 0$; the different longitudinal modes appear as dark stripes in the grey scale data. Experimentally measured energies of the polariton condensates are shown as red circles, clearly not matching the slope of the weak-coupling theory. **c**, Simulated reflectivity (RCWA) as a function of cavity length for cavities in the strong-coupling regime (grey scale), where the full refractive index dispersion $n = n(\lambda)$ and $k = k(\lambda)$ is used, as obtained from ellipsometry of the polymer layer. The experimentally measured energies of the polariton condensates are overlaid as red circles. In order to account for the 2D nature of the simulation, which neglects the vertical guiding layer structure that results in a lower effective refractive index, the theoretical curves are shifted slightly ($+0.07 \mu\text{m}$ in cavity length) to achieve a good match with the experiment.

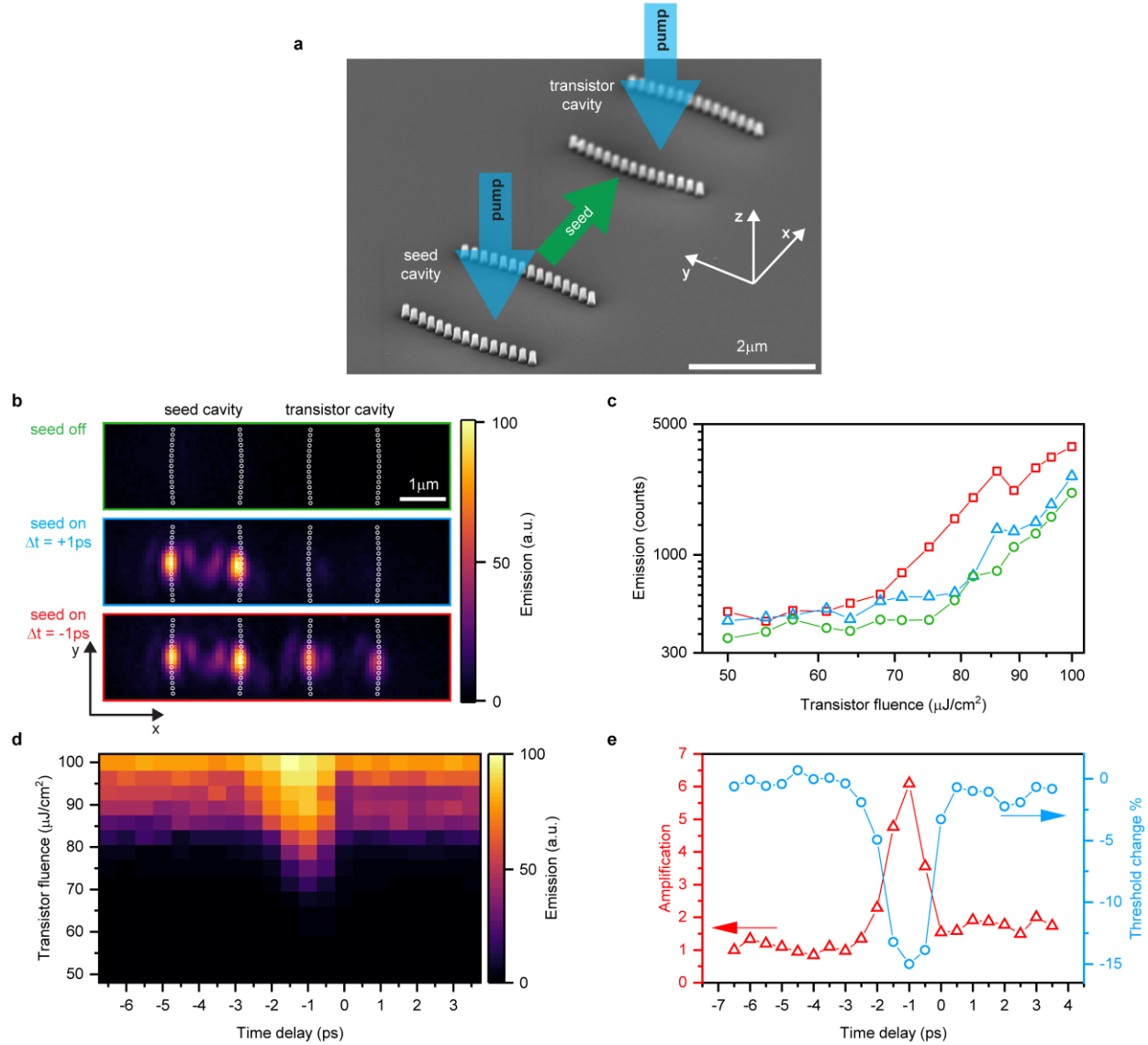


Fig. 3 | Ultrafast transistor action. **a**, Illustration where a scanning electron microscopy image of the seed and the transistor cavities is overlaid with arrows for the excitation beams and the output of the seed cavity flowing to the transistor cavity. **b**, Real space images of the emission with excitation of the transistor cavity at $P_{\text{transistor}} = 0.8 P_{\text{th}}$. In the top green panel, the seed cavity is not excited. In the middle blue panel, it is excited with $P_{\text{seed}} = 1.2 P_{\text{th}}$ at a time delay of $\Delta t = +1$ ps after the excitation of the transistor cavity. In the bottom red panel, $P_{\text{seed}} = 1.2 P_{\text{th}}$ at $\Delta t = -1$ ps before the excitation of the transistor cavity is used. **c**, Integrated intensity of emitted spectrum collected from the output mirror of the transistor cavity shown as a function of transistor excitation fluence when the transistor cavity is excited at $P_{\text{transistor}} = 0.8 P_{\text{th}}$ and the seed cavity is not pumped (green), is excited with $P_{\text{seed}} = 1.2 P_{\text{th}}$ at a time delay of $\Delta t = +1$ ps (blue) and with $P_{\text{seed}} = 1.2 P_{\text{th}}$ at a time delay of $\Delta t = -1$ ps (red). **d**, Map of the transistor output emission intensity versus transistor excitation fluence and delay time between seed and transistor excitation for $P_{\text{seed}} = 1.5 P_{\text{th}}$. **e**, Threshold reduction of the transistor cavity (blue) and amplification of the seed (red) as a function of seed–transistor excitation time delay.

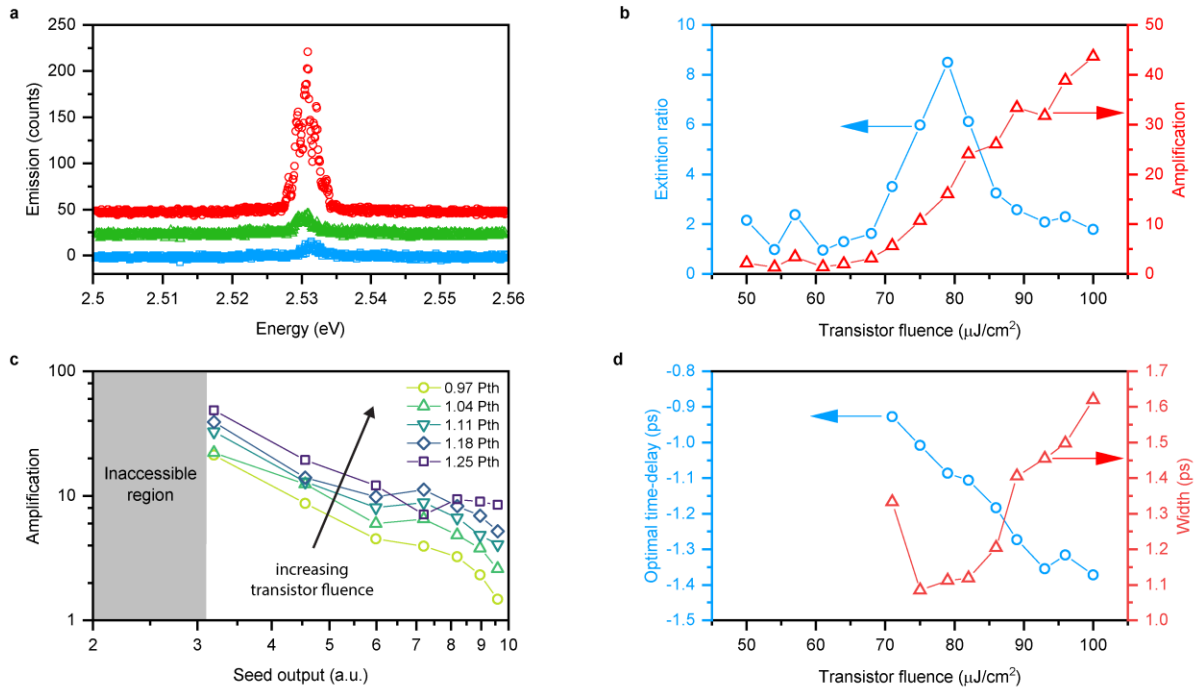


Fig. 4 | Spectra and transistor performance. **a**, Comparison between the input signal (blue), the transistor output spectrum without amplification (green) and the amplified signal (red), offset vertically by 25 counts each. The spectra have been collected at the transistor output mirror when the seed is excited with $P_{\text{seed}} = 1.2 P_{\text{th}}$ and the transistor with $P_{\text{transistor}} = 0.6 P_{\text{th}}$ (blue) and the transistor with $P_{\text{transistor}} = 1.4 P_{\text{th}}$ at $\Delta t = +1$ ps ('wrong' timing, green) and $\Delta t = -1$ ps ('right' timing, red), respectively. **b**, Amplification (red) and extinction ratio (blue) of the transistor versus transistor excitation fluence. **c**, The transistor amplification varies as a function of the intensity of the input signal, i.e. the seed cavity output which is related to the seed excitation fluence, and with the transistor excitation fluence. In the inaccessible region, the seed cavity excitation is too weak to induce polariton condensation in the seed cavity thereby preventing generation of a short input pulse to the transistor. **d**, Optimal time delay (blue) and width of the amplification time-window (red) as function of the transistor fluence.

METHODS

Device fabrication

We have fabricated the HCGs on SOI wafers with 220 nm top-Si thickness and 3 μm buried oxide using high-resolution silicon photonics technology, where electron beam lithography (Raith EBPG 5200) exposes hydrogen silsesquioxane (HSQ) resist with 200 nm layer thickness. After development with tetramethylammonium hydroxide (TMAH), the structures have been transferred by Cl-based reactive ion etching (RIE) into the top-Si layer. This results in a grating post diameter of 110 nm and a pitch of 170 nm. Methyl-substituted ladder-type poly(p-phenylene) (MeLPPP; $M_n = 31,500$ (number averaged molecular weight), $M_w = 79,000$ (weight averaged molecular weight)) was synthesized as described elsewhere⁴⁰. MeLPPP is dissolved in toluene and spin-coated on the fabricated HCG structures, resulting in approximately 220 nm layer thickness, verified by profilometry and ellipsometry. A 20 nm-thick encapsulation layer of Al_2O_3 is evaporated on top for protection against photodegradation.

Photonic simulations

For the computation of the HCG reflectivity and the spectra of the empty cavity and filled with polymer, we perform rigorous coupled wave analysis (RCWA) using a freely available software package⁴¹. For the three-dimensional finite-difference time-domain (3D FDTD) simulations, we use the commercial software ANSYS Lumerical. For both calculations, we use the complex refractive index of the polymer material obtained from variable-angle spectroscopic ellipsometry measurements (Woollam VASE) of a test polymer layer on a silicon wafer.

Optical characterization

We mount the 20 x 20 mm substrates, each containing hundreds of HCG cavities, on an *XYZ* nanopositioning stage in ambient conditions. Ultrafast excitation light pulses of 400 nm wavelength, 150 fs pulse duration and 1 kHz repetition rate are generated from a frequency-doubled regenerative amplifier that is seeded by a mode-locked Ti:sapphire laser. For the cavity detuning experiments with single HCG cavities, we insert the pulsed light into a photonic crystal fiber that stretches the pulse duration to >5 ps and provides a near-Gaussian beam at its output. The light is focused through a microscope objective (Mitutoyo Plan Apo 100X, NA=0.7) to an approximately Gaussian spot size of $\sim 3 \mu\text{m}$ $1/e^2$ diameter on the sample. For the experiments on the single cavity condensate dynamics and with multiple HCG cavities, we split the beam from the laser system and control the power and relative delay between the two beam paths before jointly inserting them into the same objective. Excitation fluences are controlled by spatially moving metallic gradient filters on linear stages. For detection, we collect the emitted light through the same objective and separate it with a dichroic beam splitter and a long pass filter from the excitation light. We route the emitted light with a 50:50 beam splitter to a camera and a monochromator with liquid nitrogen-cooled detector. The spectrometer collects the light via a multimode fiber with 10 μm diameter from an effective detection spot of $\sim 1 \mu\text{m}$ diameter on the sample for the transistor measurements and 100 μm fiber diameter with detection spot of $\sim 10 \mu\text{m}$ diameter for the other measurements.

Data availability

Data supporting the findings of this study are available from the corresponding authors upon reasonable request.

Acknowledgements

We thank the team of the IBM Binnig and Rohrer Nanotechnology Center, Daniele Caimi and the Quantum Photonics team for support with the sample fabrication and Pavlos Lagoudakis for stimulating discussions. We acknowledge funding from EU H2020 EIC Pathfinder Open project “PoLLoC” (Grant Agreement No. 899141) and EU H2020 MSCA-ITN project “AppQInfo” (Grant Agreement No. 956071).

Author contributions

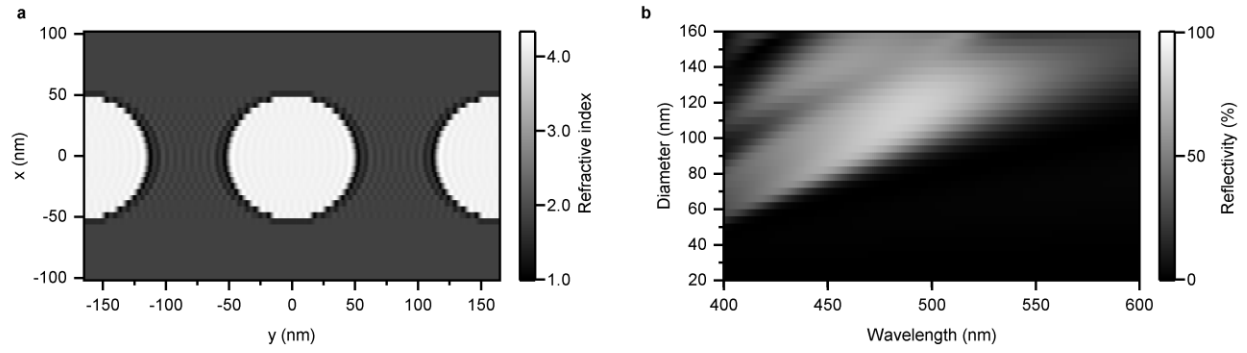
P.T. performed the experiments and analysed the experimental data, supported by D.U., B.C., J.B., T.W. and M.C.L. fabricated the silicon photonic structures. M.F. and U.S. synthesized the polymer. P.T. deposited the polymer and encapsulation layer, supported by D.U., and D.U. characterized the layers. D.U. performed the photonic simulations and designed the sample, supported by T.S., R.F.M., T.S. and D.U. conceived the concept and supervised the work. P.T., R.F.M., D.U. and T.S. wrote the paper with contributions from all authors.

Competing interests

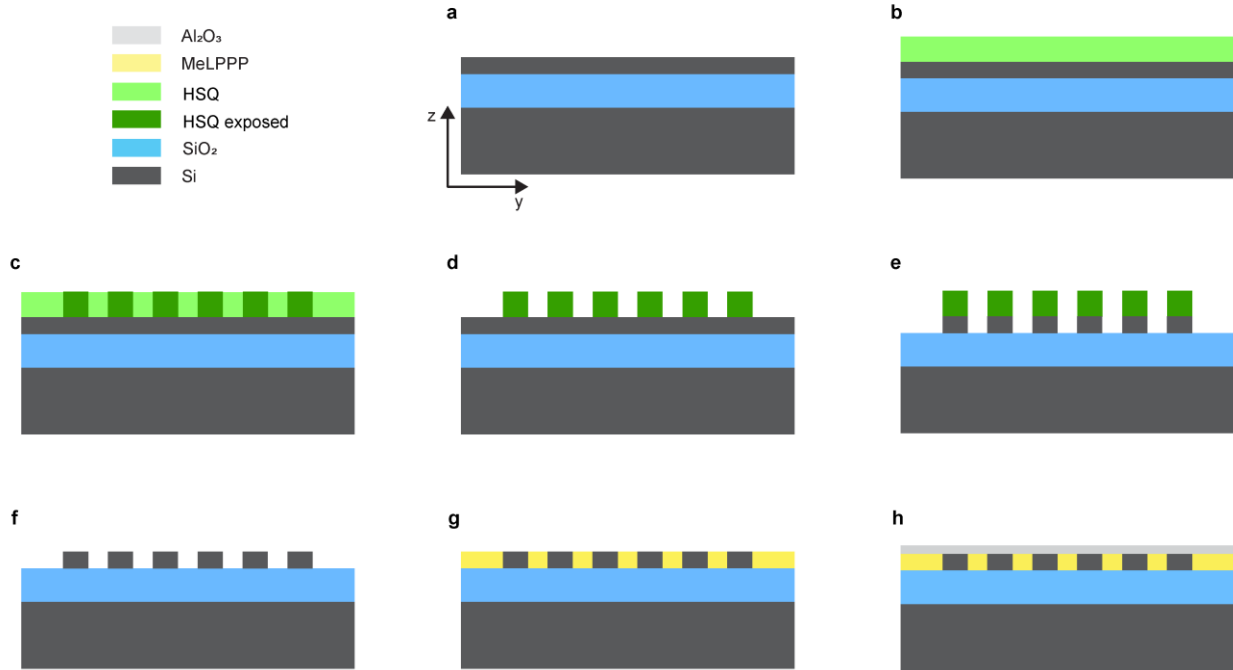
The authors declare no competing interests.

Additional information

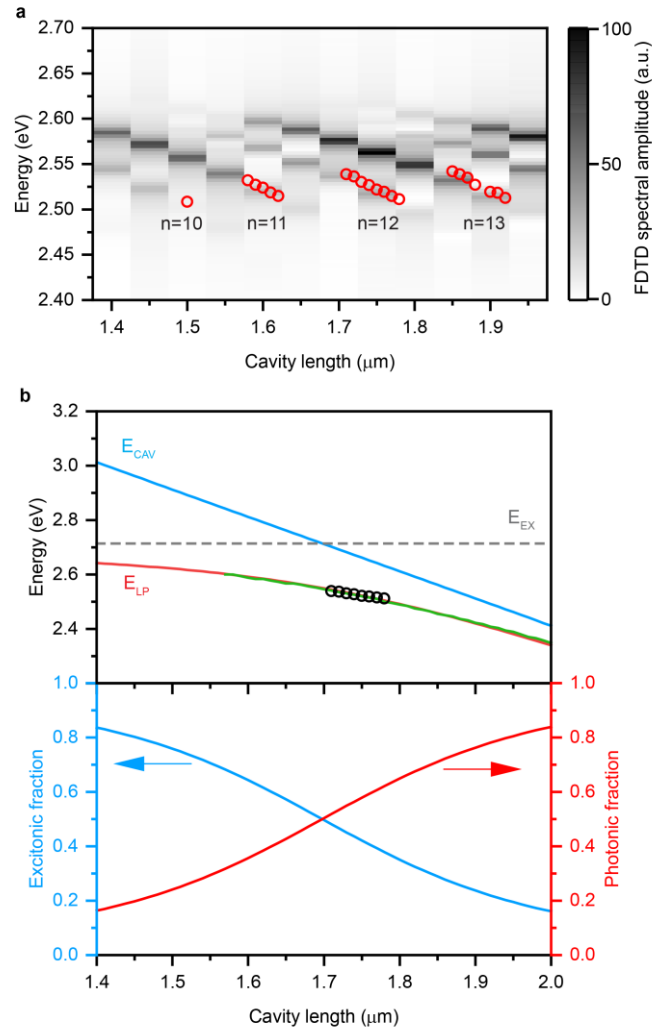
Correspondence and requests for materials should be addressed to dar@zurich.ibm.com and tof@zurich.ibm.com.



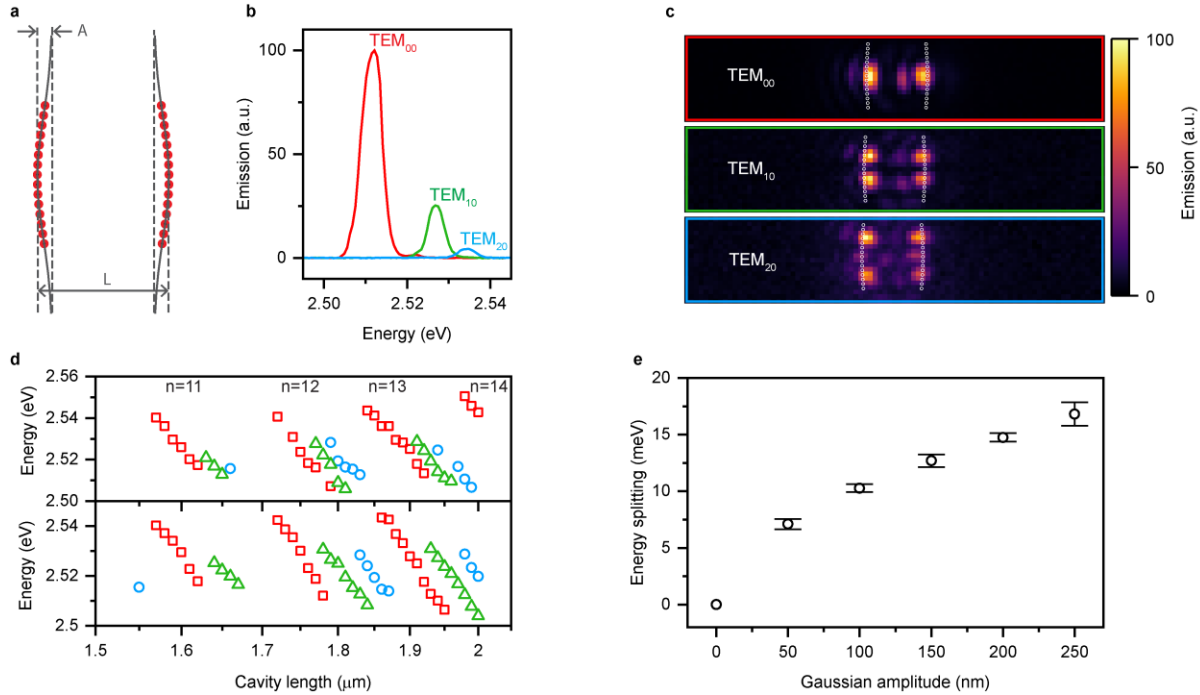
Extended Data Fig. 1 | High contrast grating mirrors. **a**, Map showing the spatial distribution of the refractive index along a silicon–MeLPPP HCG as used with the RCWA simulation. **b**, Reflectivity map of a HCG mirror as function of wavelength and the diameter of the silicon pillars constituting the grating.



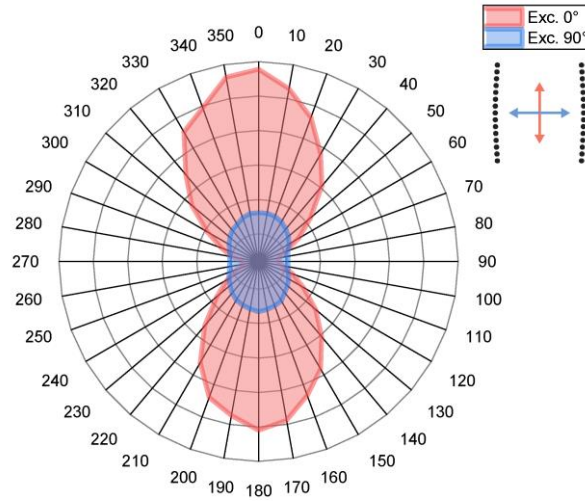
Extended Data Fig. 2 | Fabrication process of high contrast grating microcavities. **a**, SOI wafer with top silicon layer of 220 nm and 3 μm thick silica layer. **b**, Spin-coating deposition of hydrogen silsesquioxane (HSQ) resist. **c**, Exposure and patterning of HSQ with electron beam lithography. **d**, Development of HSQ. **e**, Etching uncovered silicon. **f**, Removing residual HSQ. **g**, Spin-coating deposition of MeLPPP. **h**, Encapsulation with alumina through electron beam deposition.



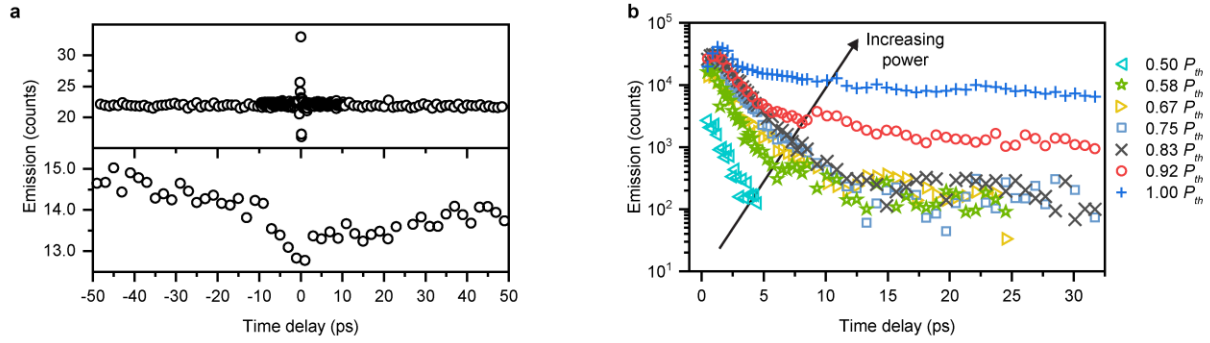
Extended Data Fig. 3 | Simulations and coupled-oscillators model. **a**, Cavity detuning plot (energy versus cavity length) of experimentally measured polariton condensation energies (red circles) and simulated spectral resonances (grey scale), designated by their longitudinal order n , as obtained from 3D FDTD calculations of HCG cavities in the strong light-matter interaction regime. The ab-initio simulations use the as-designed geometrical parameters and the measured refractive index dispersion from MeLPPP without any adjustments made to match to the experimental resonances. **b**, Top panel shows the experimentally measured resonance energies of the longitudinal mode with $n = 12$ (black circles) and a fit with a coupled-oscillators model showing the lower polariton branch (red). Cavity resonance energies displaying the strong light-matter interaction regime (green) and the weak-coupling regime (blue) have been extracted from RCWA simulations versus cavity length. The bottom panel shows the exciton (blue) and photon (red) fraction, i.e. Hopfield coefficients, of the lower polariton branch versus the cavity length for this mode.



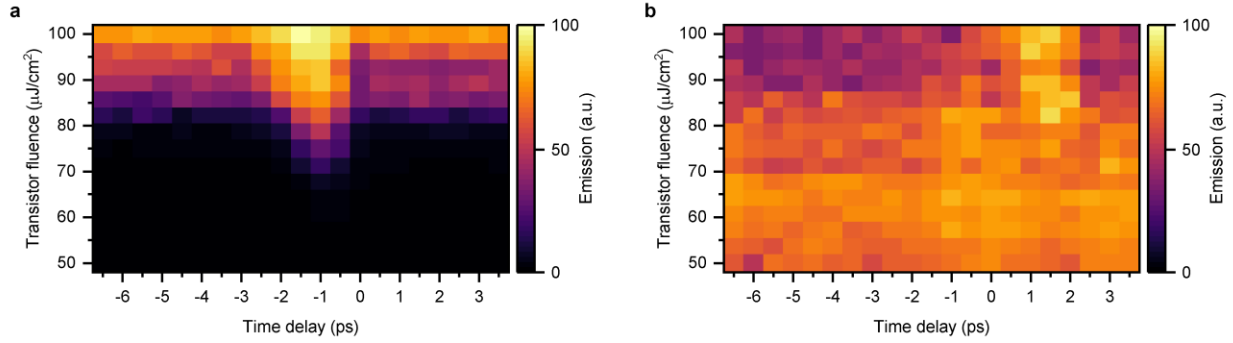
Extended Data Fig. 4 | Engineering the high contrast grating cavity modes. **a**, Scheme of a HCG cavity, highlighting the Gaussian curvature of the mirrors. **b**, Three energy-filtered emission spectra from a HCG cavity with cavity length $L = 1.92 \mu\text{m}$ and curvature described by a Gaussian amplitude of $A = 100 \text{ nm}$ and a FWHM of $2.36 \mu\text{m}$. The spectra relate to modes of different transversal order: TEM_{00} (red), TEM_{10} (green), TEM_{20} (blue). **c**, Real-space images displaying the energy-filtered emission for the three modes shown in **a** with their characteristic scattering pattern on the HCG mirrors that reflects the modal profile in the cavity. **d**, Energy of cavity resonances as a function of cavity length for 100 nm (top panel) and 250 nm (bottom panel) Gaussian-shaped cavities. Different transversal orders are highlighted by different colors and symbols with TEM_{00} (red), TEM_{10} (green), TEM_{20} (blue). **e**, Energy splitting between TEM_{00} and TEM_{10} as a function of Gaussian amplitude. For the flat cavities ($A = 0 \text{ nm}$), there is no splitting as there are no discrete transversal orders. Vertical bars indicate the standard deviations of the energy splitting resulting from measurements on different devices having different cavity lengths.



Extended Data Fig. 5 | Polarization of the emission. Emission of the HCG cavity is shown as a function of angle of a polarizer that is placed in the detection path. When the excitation polarization is aligned parallel to the HCG gratings (red), polariton condensation occurs in the cavity with a mode polarization that is parallel to the HCG gratings. When excited with the same fluence but with orthogonal polarization (blue), no polariton condensation takes place, and the emission shows an almost angularly invariant pattern, typical for the unpolarized photoluminescence from a MeLPPP film, presumably slightly modified by the scattering from the HCG gratings.



Extended Data Fig. 6 | Time delay calibration and polariton condensation dynamics. **a**, The top panel shows the intensity versus time delay for the reflections of two overlapping excitation beams (~ 150 fs duration), where interference is observed around 0 ps, that is then used as zero calibration point for the dynamical measurements. The bottom panel shows the photoluminescence intensity versus time delay between two overlapping excitation beams for an MeLPPP film without cavity, where the intensity shows a minimum around 0 ps due to nonlinear quenching from exciton annihilation. Notably, the quenching reduces with a ~ 20 ps time constant, in line with the exciton lifetime for this material. **b**, Integrated intensity of emission spectra resulting from the excitation of two spatially overlapping beams on a single HCG cavity as function of time delay for different excitation power (same fluence is used for both beams).



Extended Data Fig. 7 | Reversing the roles of seed and transistor cavity. a, Real-space emission intensity integrated over the transistor cavity area versus transistor excitation fluence and delay time between seed ($P_{\text{seed}} = 1.5 P_{\text{th}}$) and transistor excitation, showing a maximum around -1 ps delay time. **b,** Same experiment as **a**, but here the emission intensity is integrated over the seed cavity area, showing a maximum near +1 ps delay time.